51st AIAA Aerospace Sciences Meeting including the New Horizons Forum and Aerospace Exposition
07 - 10 January 2013, Grapevine (Dallas/Ft. Worth Region), Texas

AIAA 2013-1181

Method to Measure Flame Index in a Partially-Premixed Gas Turbine Combustor

David A. Rosenberg[*], Patton M. Allison[†], and James F. Driscoll[‡]
University of Michigan, Ann Arbor, Michigan, 48109, U.S.A.

This paper describes a new method to image the flame index in turbulent, partially-premixed flames. The flame index indicates the locations where premixed flames and where non-premixed flames exist. This information is needed to improve the modeling of gas turbine combustors. Using simultaneous acetone and NO_2 Planar Laser-Induced Fluorescence (PLIF), flame index was measured in a gas turbine model combustor. The fluorescence linearity and saturation characteristics of acetone and NO_2 with respect to volume fraction and laser spectral irradiance also were studied.

I. Introduction

Many modern combustion applications—gas turbines in particular—involve combustion in which the fuel and oxidizer are not completely mixed prior to entering the flame. These partially-premixed flames have some regions that contain premixed combustion and some that contain non-premixed combustion. The Takeno flame index[1] has been suggested as an indicator of how much a flame is premixed and how much is non-premixed. The flame index is defined as:

$$G_{FO} = \nabla Y_F \cdot \nabla Y_O, \tag{1}$$

where G_{FO} is the flame index and Y_F and Y_O are the fuel and oxidizer mass fractions, respectively. A flame is locally premixed when the flame index is positive, and locally non-premixed when the flame index is negative. More recently, G_{FO} has been normalized in the modeling studies of Fiorina et al. and others.[2,3] This normalized flame index, ξ, has been defined as:

$$\xi = \frac{\nabla Y_F \cdot \nabla Y_O}{|\nabla Y_F \cdot \nabla Y_O|}, \tag{2}$$

which is dimensionless. In premixed regions, $\xi = +1$, while $\xi = -1$ in non-premixed regions.

In computational models the flame index concept is useful in allowing the modeler to divide a partially-premixed flame into premixed and non-premixed reaction zones, where the appropriate combustion model can be applied.[4] There have been several studies that modeled the subgrid flame index to be a function of the resolved scale gradients of fuel and oxygen concentrations,[2–8] however no study has been performed to experimentally verify these models by measuring the fuel and oxidizer gradient. Models of partially-premixed flames need to correctly predict the flame index, so measurements are needed to assess the models.

The flame index measurements described in this paper were taken in a well-studied gas turbine model combustor (GTMC) developed by Meier and colleagues at DLR Stuttgart. The burner is of canonical axisymmetric swirler-design yet it exhibits the fundamental physics associated with gas turbine flames; it contains two swirling air streams that surround an annular fuel stream. Comprehensive measurements have been conducted to investigate flame-structure, flame-dynamics, and flow-field structures for a few selected methane-fueled conditions.[9–11] However, flame index has not been experimentally measured in this, or in any combustor. The condition studied in this paper is similar to the conditions studied previously.

II. Experiment

A. Combustor and flame conditions

The experimental methods described previously[12] have been applied to a gas turbine model combustor (GTMC), pictured in Fig. 1.[10,11] The injector consisted of a central air nozzle, an annular fuel nozzle, and a co-annular air nozzle. Both air nozzles supplied swirling air at atmospheric pressure and temperature from a common plenum. The inner air nozzle had an outer diameter of 15 mm and the annular nozzle had an inner diameter of 17 mm and an outer

---

[*]Graduate Research Assistant, Department of Aerospace Engineering, AIAA Member, davidaro@umich.edu
[†]Graduate Research Assistant, Department of Aerospace Engineering, AIAA Member, pallison@umich.edu
[‡]Professor, Department of Aerospace Engineering, AIAA Fellow, jamesfd@umich.edu

American Institute of Aeronautics and Astronautics

diameter of 25 mm. The measured swirl number was approximately 0.55. Non-swirling fuel was provided through three exterior ports fed through the annular nozzle, which was subdivided into 72 channels with a 0.5 mm × 0.5 mm cross section. The exit plane of the central air nozzle and fuel nozzle lay 4.5 mm below the exit plane of the outer air annulus. The exit plane of the outer air annulus will be referred to as the injector face. The combustion chamber had a square cross section of 85 mm in width and 110 mm in height. The exit of the combustion chamber was an exhaust tube with a diameter of 40 mm and a height of 50 mm. In the present investigation, the burner was operated with four fused silica windows, with a thickness of 1.5 mm, for flame visualization.

The air was seeded with NO_2, while the CH_4 was seeded with acetone. The NO_2 seeding was achieved by using a premixed gas cylinder. The acetone seeding in the CH_4 was achieved by bubbling the CH_4 through an acetone bath. The bath had a bypass line, through which the flow of CH_4 could be controlled. Heat tape, connected to a PID temperature controller, kept the acetone in the bath at a constant temperature $\pm 2°C$ to more precisely control the acetone concentration.

Using the GTMC the flame index was measured in a CH_4/acetone/air flame for run conditions that are similar to the conditions of flame B studied by Weigand et al.[10] The difference being that NO_2 and acetone were added in the present work. The conditions are described in Table 1.
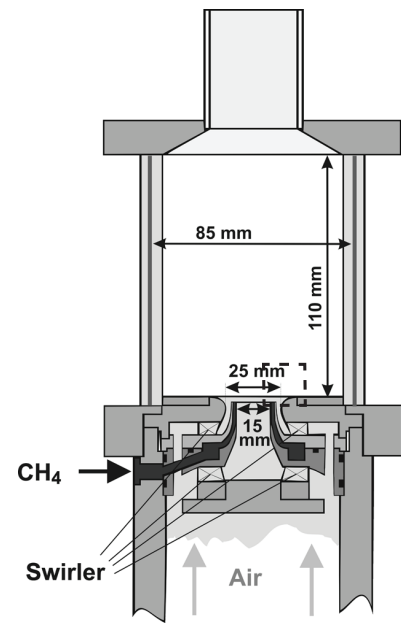

Figure 1. Cross-sectional view of gas turbine model combustor designed by Meier et al.[10] The dashed box shows the field of view used in the experiment.

Table 1. Flame conditions. The flow rate of species i is $\dot{m}_i$, and ϕ_{global} is the equivalence ratio for the overall mixture.

$\dot{m}_a$, g/min[a]	$\dot{m}_f$, g/min[b]	ϕ_{global}	NO_2 Volume Fraction[c]	Acetone Volume Fraction[c]
285	16	0.76	5,000 ppm	21.0%

[a] Includes air and NO_2.

[b] Includes CH_4 and acetone.

[c] Volume fractions are for the pure fuel or pure air stream, by volume.

B. Planar laser-induced fluorescence system

As suggested by prior studies[13–15] and the previous flame modeling study,[12] acetone makes an excellent fuel tracer. It fluoresces in the wavelength range between 400 nm and 500 nm when excited by a 266 nm laser. While NO_2 is not traditionally considered to be an oxygen tracer, the models showed that NO_2 will function as such. Agarwal et al.[16] showed that NO_2 will fluoresce from 540 nm to 675 nm when excited by a 488 nm Argon-Ion laser, while Donnelly et al.[17] showed that NO_2 will fluoresce from 550 nm to wavelengths longer than 800 nm when excited by a 532 nm Nd:YAG laser. Cattolica[18,19] has shown that applying NO_2 planar laser-induced fluorescence (PLIF) to combustion studies is possible.

A diagram of the layout of the lasers, cameras, and burner for the simultaneous acetone and NO_2 PLIF system can be seen in Fig. 2. The NO_2 PLIF was achieved with a frequency doubled Nd:YAG laser (Spectra Physics LAB-150, Laser #1) operated at a wavelength of 532 nm. The acetone PLIF was achieved with a frequency quadrupled Nd:YAG laser (Spectra Physics GCR-130, Laser #2) operated at a wavelength of 266 nm. Both lasers had a linewidth of approximately 1.0 cm^{-1}. The 266 nm laser has a pulse width of about 6 ns, while the 532 nm laser had a pulse width of approximately 8 ns. The 266 nm laser had an energy of 30 mJ/pulse, and the 532 nm laser was operated at 110 mJ/pulse. At the burner the 266 nm laser energy had been reduced to 10 mJ. The normalized spectral irradiance was 40 $MW/cm^2/cm^{-1}$. The 532 nm laser energy had been reduced to 45 mJ, and the normalized spectral irradiance was 290 $MW/cm^2/cm^{-1}$. Both lasers were pulsed at a rate of 10 Hz. Over time the power and shape of the 266 nm laser beam tended to degrade, so it was decided to correct for the non-uniformities in the laser sheet on a shot-to-shot basis using a dye cell.

The laser beams were formed into sheets using two cylindrical lenses and were passed between knife edges, set
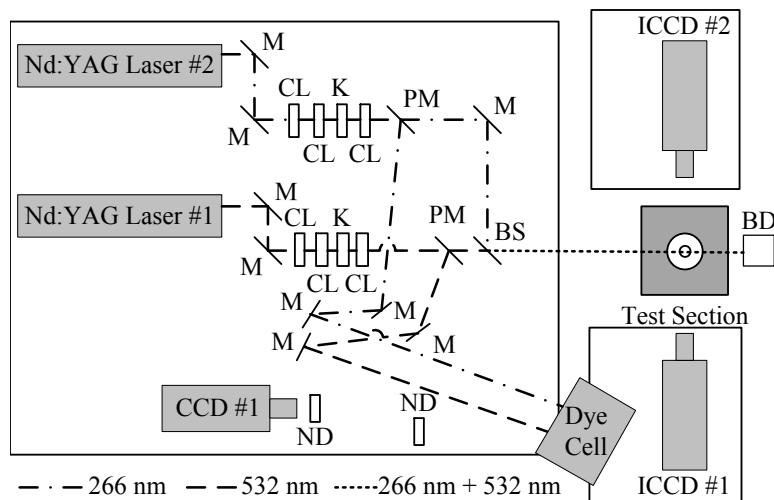
Figure 2. Diagram of laser and camera setup for simultaneous PLIF. BD - beam dump, BS - beam splitter, CL - cylindrical lens, K - knife edge, M - mirror, ND - neutral density filter, PM - partial mirror.

10 mm apart, to chop the top and bottom of the laser sheets. They next passed through 10% pick-off mirrors to a dye cell with an optically thick Rhodamine 6G solution to correct for the non-uniformity of the laser sheet. The distances were set up such that the laser sheets would be focused inside the dye cell. The remaining 90% of the laser sheets were then combined using a dichroic beam splitter (CVI Melles Griot BSR-25-2025) and passed through the burner. At the test section the 266 nm laser sheet had a height of 10 mm and a $1/e$ thickness of 250 μm at its focal point. At the same location the 532 nm laser sheet had a height of 10 mm and a $1/e$ thickness of 200 μm. The knife edge was used to create a sharp edge in the observed PLIF signals and the fluorescence observed in the dye cell, so that the two images could later be aligned, as suggested by Clemens.[20]

NO$_2$ fluorescence was observed by a red-sensitive intensified CCD (ICCD) camera (Andor iStar DH334T-18U-A3, ICCD #1) with an interference filter (CVI Melles Griot LPF-600) and two 3 mm thick color filters (Schott OG-550) to allow light with wavelengths 600 nm and longer to pass through. Observing the NO$_2$ fluorescence using a red-sensitive ICCD, with a third generation intensifier, was necessary to achieve the maximum possible signal-to-noise ratio. The acetone fluorescence also was observed by an ICCD camera (Andor iStar DH734-25F-03, ICCD #2) with an interference filter (Omega Optical 500ASP) to allow light at wavelengths of 400 nm to 500 nm to pass. Each camera was fitted with a 105 mm f/2.8D Micro-Nikkor lens. A CCD camera (Sony XCD-X710, CCD #1) was fitted with a 50 mm f/2.8 Nikkor lens. It imaged the dye cell for shot-to-shot corrections to the non-uniformity of the laser sheets. A neutral density (ND) filter, with an optical density of 2, was placed to cover only the half of the dye cell that the 532 nm laser sheet hit. A second ND filter, with an optical density of 1, was placed to cover the entire dye cell image. The dye cell camera had an exposure time of 3 ms, and it captured the fluorescence from both of the laser sheets in that time.

To ensure that the NO$_2$ camera's gate was fully open, the intensifier gated to turn on 50 ns before the arrival of the 532 nm laser pulse. The intensifier gain on the NO$_2$ camera was turned up to the maximum possible level. The acetone camera's intensifier was gated to turn on 50 ns before the arrival of the 266 nm laser pulse. Both cameras operated with a 100 ns intensifier gate width. A total of 450 images were taken by each camera.

There is some overlap between the fluorescence spectra of acetone and NO$_2$ that the optical filters on the cameras did not filter out. If nothing had been done, some of the acetone fluorescence would have been seen on the NO$_2$ camera. As a result, the lasers were timed such that the 266 nm laser pulse reached the burner 500 ns before the 532 nm laser pulse.

The cameras each had an array of 1024 $\times$ 1024 pixels. The resolution was 20 $\pm$ 7.2 μm/pixel for the NO$_2$ camera, and 21 $\pm$ 7.6 μm/pixel for the acetone camera.

On a daily basis several calibration steps had to be taken. The laser sheets were checked to be sure they overlapped and passed through the center of the burner. The camera timing was tuned to be sure both the NO$_2$ and acetone PLIF camera gates opened 50 ns before the arrival of their respective laser pulses. Finally, the cameras were both focused on a targeting grid, which had been aligned with the laser sheets, and field-of-view images of the target were taken with each camera so that the images could later be registered.

After each day of runs a series of background images was taken. One series of images recorded the flame seeded with NO$_2$ and acetone but with the lasers turned off. Additional images recorded the flame without the tracer gas

a given camera looks for but with the other tracer gas present (e.g., a flame without NO_2 seeding but with acetone seeding, imaged by the NO_2 camera), with the lasers on. A final set of images recorded the same flame without the lasers. Typically, each camera would capture 20 images for each of the background conditions. The theory behind the image corrections that require the background and dye cell images is described in Appendix A.

III.   Fluorescence Linearity and Saturation Study

To determine the optimal energy of the lasers, the linearity and possible saturation limits of both acetone and NO_2 were studied. The NO_2 calibration was performed using the same setup described above, while the acetone calibration was performed with the setup described previously.[12] In both cases only the CH_4/acetone mixture or the air/NO_2 mixture flowed through the test chamber, which was at a pressure of 1 atm and a temperature of 293 K. Each data point represents the average fluorescence intensity over 30 laser pulses. Laser energies were measured with a calibrated pyroelectric power meter. Laser energies are provided in both the energy, in mJ/pulse, observed at the burner, and in the normalized spectral irradiance, in MW/cm^2/cm^{-1}, as suggested by Partridge and Laurendeau.[21]

a) Acetone calibration with varying laser energy. Acetone was at a volume fraction of 13% in CH_4, at a pressure of 1 atm, and a temperature of 293 K.

b) NO_2 calibration with varying laser energy. NO_2 was at a volume fraction of 5,000 ppm in air, at a pressure of 1 atm, and a temperature of 293 K.
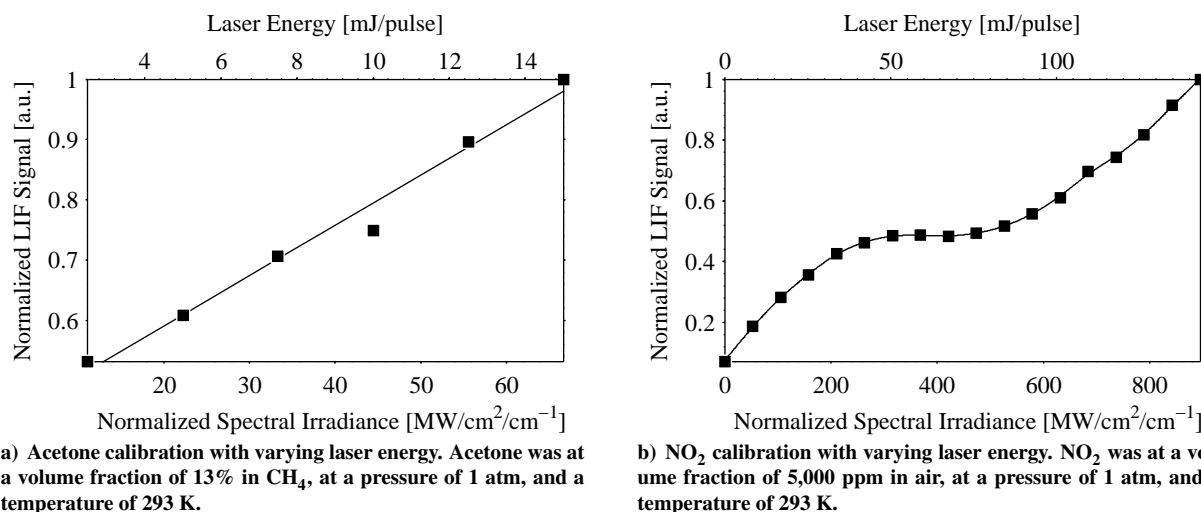
Figure 3. Fluorescence saturation study of varying laser energy for a) acetone in CH_4 and b) NO_2 in air.

The acetone laser calibration results, shown in Fig. 3a, were obtained for a mixture of 13% acetone, by volume, in CH_4 over the range of possible energy outputs by the laser. As was observed by Lozano et al.[13] and by Thurber and Hanson,[14] the acetone fluorescence does not saturate in this regime.

a) Acetone calibration results with varying volume fraction. Laser energy was 15 mJ. CH_4/acetone mixture was at a pressure of 1 atm and a temperature of 293 K.

b) NO_2 calibration results for varying volume fraction. Laser energy was 40 mJ and 125 mJ. Air/NO_2 mixture was at a pressure of 1 atm and a temperature of 293 K. All LIF signals have been normalized.
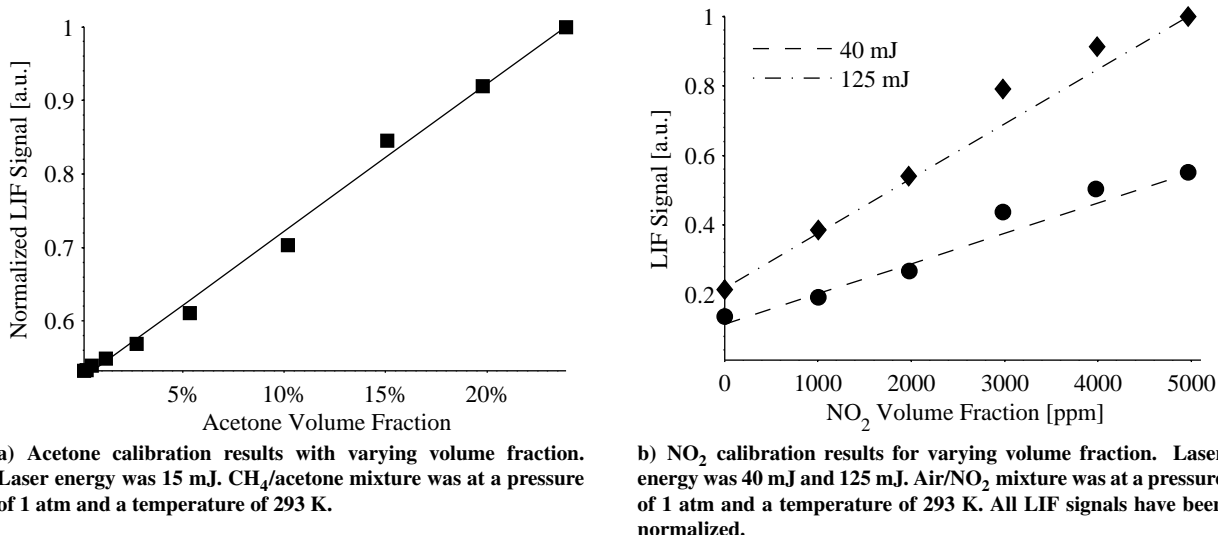
Figure 4. Fluorescence calibration results for varying volume fractions for a) acetone in CH_4 and CH_4 and b) NO_2 in air.

The NO_2 calibration results, shown in Fig. 3b, were obtained using a mixture of 5,000 ppm NO_2 in air. We can see that the NO_2 fluorescence signal is non-linear, which may mean that the NO_2 was partially saturated.

American Institute of Aeronautics and Astronautics

The results of the acetone calibration for varying volume fraction in CH_4 are shown in Fig. 4a. The study was performed at a laser energy of about 15 mJ, or approximately 125 MW/cm^2/cm^{-1}. It can be seen that the acetone signal varies linearly with volume fraction and, in this regime, does not saturate.

The results of the NO_2 calibration for varying volume fraction in air are shown in Fig. 4b. The study was performed at a laser energy of 40 mJ and at 125 mJ, or 250 MW/cm^2/cm^{-1} and 800 MW/cm^2/cm^{-1}. It can be seen that NO_2 fluorescence responds linearly to variations in the NO_2 volume fraction in air.

IV.   Flame Index Measurement

Using the setup described above, 450 simultaneous acetone and NO_2 PLIF image pairs were acquired, and from each of these images a flame index could be measured. The raw acetone PLIF had a very good signal-to-noise ratio of 22, while the NO_2 PLIF had an S/N ratio of 5.

The flame index defined in Eq. (2) depends on the fuel and oxygen gradients. Our previous work[12] showed that the acetone gradients and NO_2 gradients adequately represent the fuel and oxygen, respectively so the flame index has been defined as:

$$\xi_{LIF} = \frac{\nabla S_{acetone} \cdot \nabla S_{NO_2}}{|\nabla S_{acetone} \cdot \nabla S_{NO_2}|}, \tag{3}$$

where ξ_{LIF} is the flame index based on the LIF signal. $S_{acetone}$ is the acetone fluorescence signal, and S_{NO_2} is the NO_2 fluorescence signal.

After the signal, background, and sheet correction data has been recorded, several steps were required to determine the flame index.

- Information was gathered to register the two images and to determine the location of the laser sheet within the images.

- Image corrections were made, as suggested by Clemens.[20]

- Processing of the corrected images involved:

    - Edge detection.

    - Spacial gradient calculation.

    - Flame index determination.

A.   Data Processing method

The field-of-view of each camera was determined using a focusing target. The NO_2 field-of-view image was flipped, rotated, and stretched so that it would be aligned to the acetone field-of-view image. The amounts of rotation and stretch were recorded so that the same process could be done with the NO_2 PLIF images.

B.   Image corrections and registration

After the information-gathering stage was complete, the raw PLIF images were read in. A set of typical simultaneous raw NO_2 and acetone PLIF images are shown in Fig. 5. In the images shown, the NO_2 PLIF image has not yet been registered to the acetone PLIF image, so the r-axis is flipped. A schematic of the GTMC has been overlaid on top of the image. The fuel injector, inner air swirler, and outer air swirler locations are shown in the diagrams, as well as the fuel and air paths. At the location of $r = 8$ mm is the fuel injector. The location 0 mm on the r-axis corresponds to the centerline of the burner, and the location 0 on the y-axis corresponds to the top of the injector face. The top of the fuel injector is located at -4.5 mm on the y-axis. The bottoms of both laser sheets are located about 420 μm above the injector face.

The outer edges of the acetone signal are similar to the outer edges of the NO_2 signal. This indicates that premixed flamelets, $\xi = +1$, are likely to be found. At other locations a strong acetone signal corresponds to areas of weak NO_2 signal. These are locations where non-premixed flamelets, $\xi = -1$, are likely to be found.

Figure 6 shows how the intensities of the laser sheets vary in the y-direction. These profiles were recorded by directing 10% of the laser sheet energy into the dye cell.
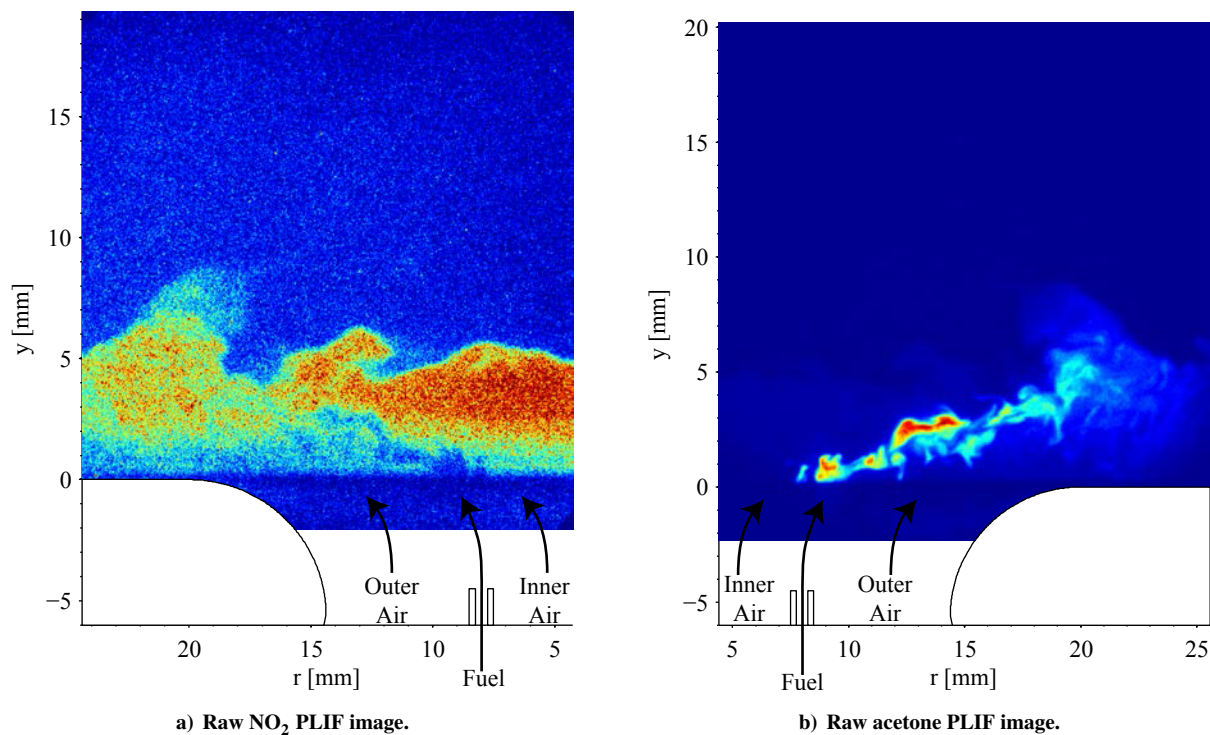
American Institute of Aeronautics and Astronautics

a) Raw NO$_2$ PLIF image.

b) Raw acetone PLIF image.

Figure 5. Sample simultaneous raw a) NO$_2$ and b) acetone PLIF images. Images are of the same field of view, however the NO$_2$ PLIF image has not been registered to the acetone PLIF image.

The process of using the background images and the dye cell images to correct the images is described in Appendix A. After image corrections had been performed, the NO$_2$ PLIF image was flipped, rotated, and stretched by the amounts previously recorded so that it was registered to the acetone PLIF image. The corrected versions of the raw PLIF images shown in Fig. 5 are shown in Fig. 7.

After the images have been corrected and registered, acetone PLIF image had an S/N of 26, and the NO$_2$ PLIF image had an S/N of 5. It is likely the NO$_2$ image exhibited an improvement in S/N, however it is difficult to select the same region of the image before and after registration to observe how the S/N increased. The acetone PLIF image was not shifted, rotated, or flipped, so the region in the raw image that was used to determine S/N is the same region used in the corrected image.
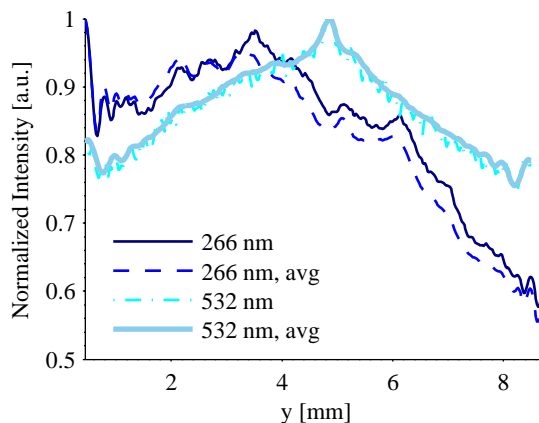

Figure 6. Variations in the intensity of both the 266 nm and 532 nm laser sheets are shown, as well as the laser sheet intensities averaged over 450 images.

1. Image pre-processing

After the acetone and NO$_2$ PLIF images had been corrected and registered, the pre-processing stage began. The purpose of the pre-processing was to improve the edge detection.

The first stage of the pre-processing was to bin the PLIF images into super-pixels, each of which consisted of 4×4 (i.e., 16) original pixels. It was decided that binning the images 4×4 was the best balance between the resolution loss and S/N gain. The S/N on the acetone PLIF image was 50, and the S/N on the NO$_2$ PLIF image was 9. The improvement is slightly less than two in both cases. The resolution for the binned images was 85 ± 14 μm/pixel. The binning converted the formerly 1024×1024 pixel images to 256×256 pixels.

American Institute of Aeronautics and Astronautics

The final pre-processing step was to spatially filter the images. The images were filtered using a non-linear anisotropic diffusion filter (NADF).[22] The NADF smooths the image within a given region, but resists smoothing the image across large gradients. NADF is excellent at preserving the edges in the image, while it helps the edge detection algorithm to avoid detecting false edges in the uniform regions. After filtering the PLIF images, the NO_2 PLIF image had an S/N of 19, while the acetone PLIF image had an S/N of 63.

After filtering was complete, the images were cropped to the region in which the two laser sheets overlapped to produce a pair of images each 96 pixels tall by 242 pixels wide. These final NO_2 and acetone PLIF images are shown in Fig. 8. The images shown are the same frames shown in Figs. 5 and 7. It can be seen that for both the NO_2 and acetone PLIF images the edges at both the outside boundary of the PLIF signals, and variations within the signal, are more clearly visible than they were in Fig. 7, before the filtering process.

The cropping of the images was held off until this last stage, rather than cropping earlier to save on computer memory. Earlier filtering tended to create false edges at the edges of the image. This was reduced when the top and bottom of the laser sheet were not located at the top and bottom of the image.

2. Image processing

After the pre-processing of the image was complete the processing itself began. It was necessary to determine the locations of large gradients in order to determine where gradients should be multiplied to measure flame index. As shown in the previous modeling study,[12] in a non-premixed flamelet, the locations of maximum gradient do not necessarily overlap. So the gradients of the acetone and NO_2 signals could not simply be multiplied at each spacial location. To solve this problem, it was necessary to develop a way to search for corresponding locations of maximum gradient. A Canny edge detector[23] was used because it identified more continuous edges than other commonly used edge detectors. Following the edge detection, the gradient at those edge locations was determined by a central differencing method.

Finally, the flame index was determined. The instantaneous flame index values for three cases are shown in Fig. 9. Figure 9a was recorded at a time when mostly premixed flamelets occur. Figure 9b shows non-premixed and premixed flamelets, as well as a premixed flamelet that has broken off and lies above the two attached flamelets. Figure 9c is from the same PLIF image shown in previous figures, and shows a progression from a non-premixed to a premixed flamelet.

Initially, the two gradient matrices were compared, and at locations where two detected edges overlap, Eq. (3) was evaluated. As the flame modeling results described previ-
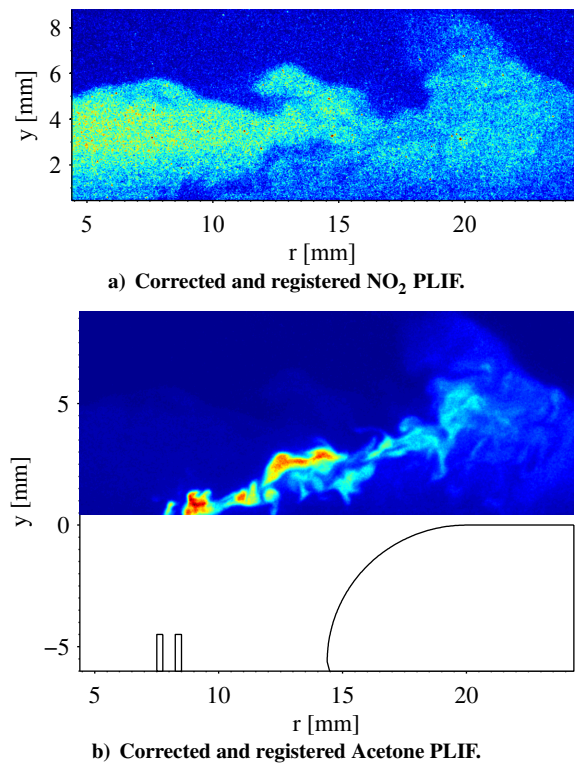

a) Corrected and registered NO_2 PLIF.

b) Corrected and registered Acetone PLIF.

Figure 7. Sample simultaneous corrected and registered a) NO_2 and b) acetone PLIF images.

a) Pre-processed NO_2 PLIF.

b) Pre-processed Acetone PLIF.
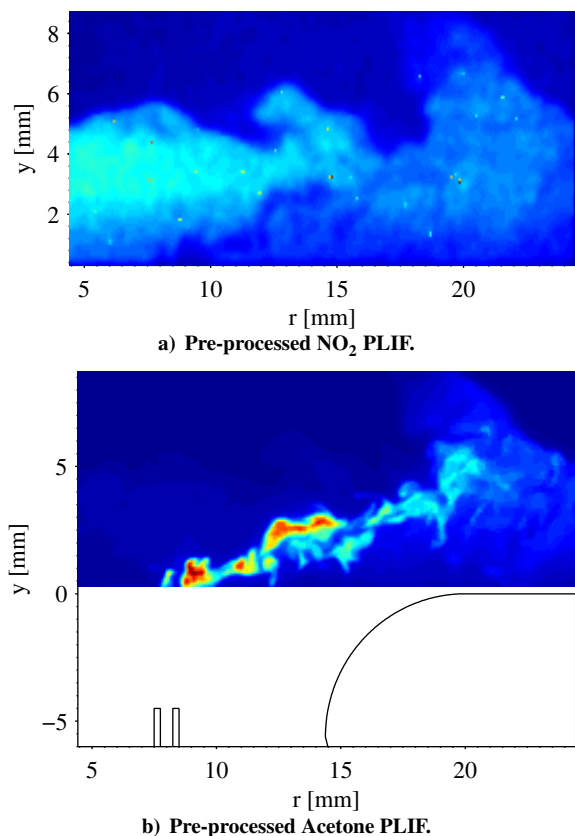
Figure 8. Sample simultaneous a) NO_2 and b) acetone PLIF images following the pre-processing phase.

American Institute of Aeronautics and Astronautics

a) Time when predominantly premixed flamelets occur.

b) Time when both non-premixed and premixed flamelets exist.

c) Time when non-premixed flamelets occur from $r = 8$ mm to 18 mm and premixed flamelets dominate at $r > 18$ mm.
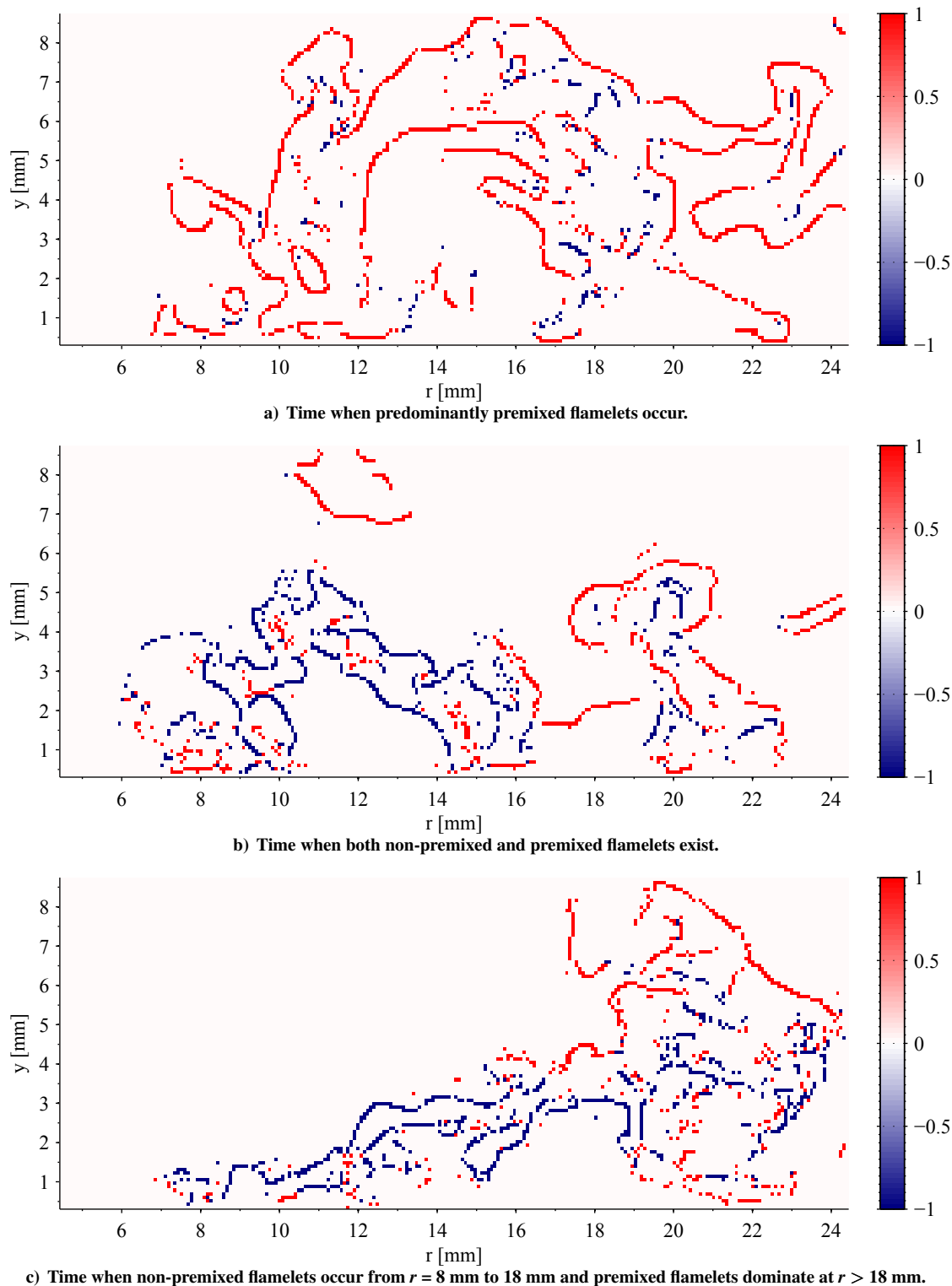
Figure 9. Three instantaneous images of flame index. A value of -1 marks a non-premixed flamelet in blue, and $+1$ marks a premixed flamelet in red.

ously[12] showed, the gradients do not overlap for a diffusion flame. So at locations where an edge had been detected in the acetone PLIF image, a search was initiated to find an edge in the NO_2 PLIF image. This was accomplished by searching both in the direction that the acetone gradient vector pointed, and in the opposite direction. This searching procedure is necessary because for premixed conditions the acetone and NO_2 gradients would point in the same direction. For non-premixed conditions the acetone and NO_2 gradients point in opposite directions, and the acetone gradient vector points away from the location where the NO_2 gradient is large. To minimize errors in the registration

process or errors in the edge detection, both premixed and non-premixed flame locations were searched for in both directions.

It was also seen in the CHEMKIN modeling results[12] that the maximum values of the acetone and NO_2 gradients would be separated by about 0.1 mm in a premixed flame, and 4 mm in an opposed-flow non-premixed flame. To avoid detecting unrelated NO_2 pixel locations, the search distance, Δs, in both directions for an NO_2 gradient that would give $\xi_{LIF} = -1$ was limited to 1 mm, while in the search for an NO_2 gradient that would give $\xi_{LIF} = -1$ Δs was limited to 0.5 mm. This alteration in search distance led to a reduction in misidentified flame index values (e.g., a pixel identified as non-premixed but surrounded by pixels identified as premixed, or pixels floating in space by themselves).

To avoid detecting unrelated NO_2 pixel locations, the search distance, Δs, in the opposite direction that the acetone vector pointed was limited to 1 mm for an NO_2 gradient that would give $\xi_{LIF} = -1$, and 0.5 mm for an NO_2 gradient that would give $\xi_{LIF} = +1$. In the direction that the acetone vector pointed, Δs was limited to 0.5 mm for an NO_2 gradient that would give $\xi_{LIF} = -1$, and 1 mm for an NO_2 gradient that would give $\xi_{LIF} = +1$. This alteration in search distance led to a reduction in misidentified flame index values (e.g., a pixel identified as non-premixed but surrounded by pixels identified as premixed, or pixels floating in space by themselves).

When a premixed flamelet is identified, the location of the flamelet is well defined to be the pixels where the maximum gradients occur. The location of a non-premixed flamelet is not so clear. The flamelet reaction zone occurs between the locations of maximum fuel gradient and maximum oxygen gradient. Therefore $\xi_{LIF} = -1$ was assigned to pixels that are halfway between the maximum NO_2 and acetone gradients. This led the most continuous lines of flame index values.

3. Flame index post-processing

With the ensemble of 450 separate frames with flame index measurements, some statistical analysis was done. To perform statistical averaging, the field of view was divided into super-pixels of size 980 ± 45.8 μm/pixel. The image was reduced from a size of 96×242 pixels down to 8×22 pixels.

For each super-pixel, a probability mass function (PMF) of ξ_{LIF} was determined for the three possible values -1, 0, and $+1$. An example PMF for a single super-pixel is shown in Fig. 10, where A is the probability that $\xi_{LIF} = +1$, B is the probability that $\xi_{LIF} = 0$, and C is the probability that $\xi_{LIF} = -1$. While the lines in the figure appear to have some thickness, in reality they are delta functions so probabilities A, B, and C are located only at -1, 0, and $+1$, respectively, and are thus infinitely thin. The sum of the areas under all three curves, $A + B + C = 1$. Contours of the PMF for the full data set are shown in Fig. 11.

Figure 10. Probability mass function of ξ_{LIF} for a single super-pixel. A is the probability that $\xi_{LIF} = +1$, B is the probability that $\xi_{LIF} = 0$, and C is the probability that $\xi_{LIF} = -1$.

Using the PMF, the average value of the flame index for each super-pixel is:

$$\langle \xi_{LIF} \rangle = \frac{(-1)A + (0)B + (1)C}{A + B + C}, \tag{4}$$

where $\langle \xi_{LIF} \rangle$ is the average flame index for that super-pixel. Because B is centered at $\xi_{LIF} = 0$ and $A + B + C = 1$, Eq. (4) can be simplified to be:

$$\langle \xi_{LIF} \rangle = C - A. \tag{5}$$

This ensemble average flame index, while useful, is not the best indicator of where premixed and non-premixed flamelets occur. A better indicator is the following conditioned average:

$$\langle \xi_{LIF} | \xi_{LIF} \neq 0 \rangle = \frac{(-1)A + (1)C}{A + C}, \tag{6}$$

where $\langle \xi_{LIF} | \xi_{LIF} \neq 0 \rangle$ is the average of ξ_{LIF}, conditioned on the condition that ξ_{LIF} is nonzero, meaning that a flamelet was present. Equation (6) can be simplified to be:

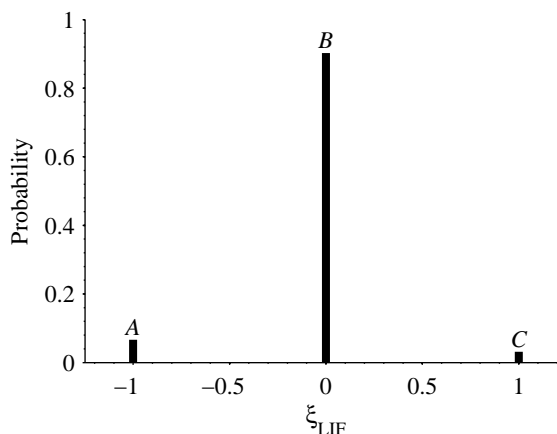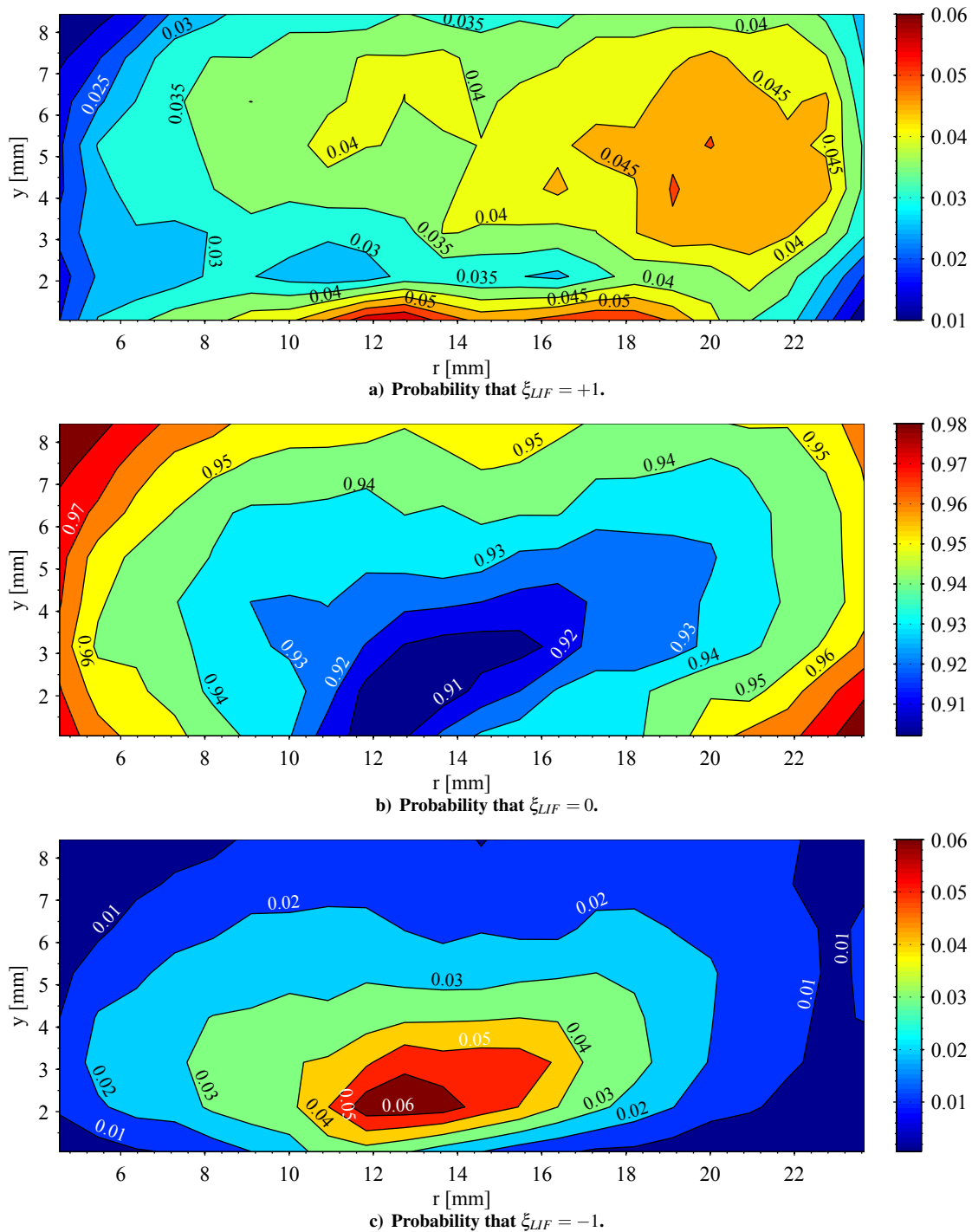$$\langle \xi_{LIF} | \xi_{LIF} \neq 0 \rangle = \frac{C - A}{A + C}. \tag{7}$$

American Institute of Aeronautics and Astronautics

a) Probability that $\xi_{LIF} = +1$.

b) Probability that $\xi_{LIF} = 0$.

c) Probability that $\xi_{LIF} = -1$.

Figure 11. The probability mass function for ξ_{LIF}.

Both the averaged flame index and the conditionally averaged flame index are shown in Fig. 12.
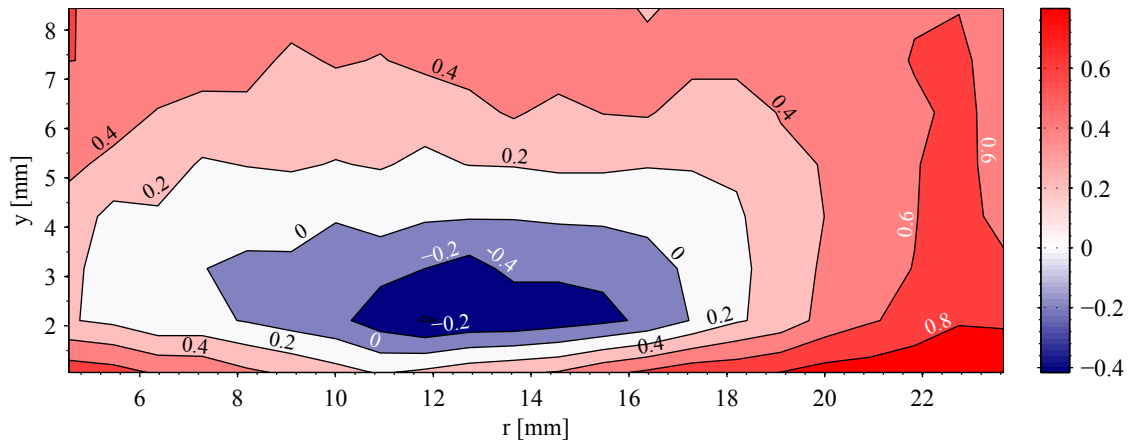
In addition to the average flame indices, the standard deviation of the flame index, $\sigma_{\xi_{LIF}}$, for a given super-pixel was calculated to be:

$$\sigma_{\xi_{LIF}} = \sqrt{A[(-1) - \langle \xi_{LIF} \rangle]^2 + B[(0) - \langle \xi_{LIF} \rangle)]^2 + C[(+1) - \langle \xi_{LIF} \rangle]^2}. \tag{8}$$

Values of the standard deviation can be seen in Fig. 13.

American Institute of Aeronautics and Astronautics
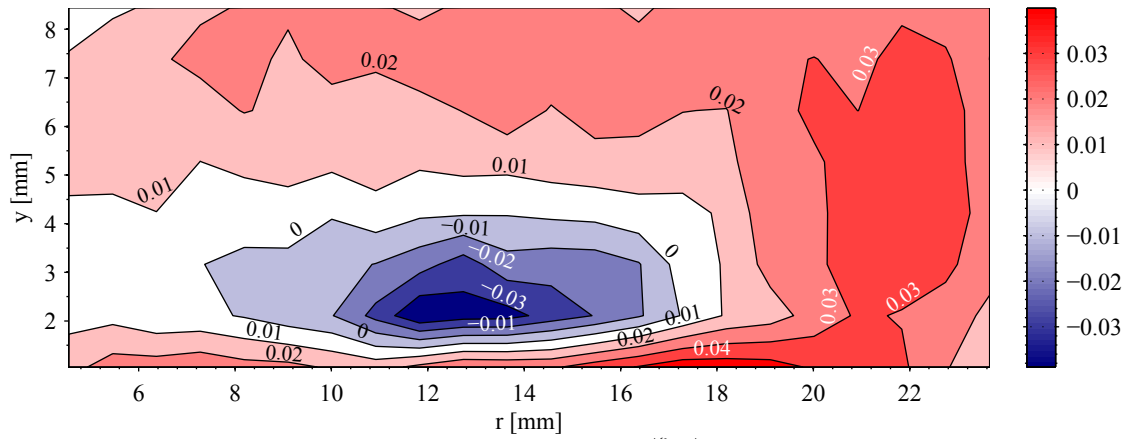
a) Averaged flame index, $\langle \xi_{LIF} \rangle$.

b) Conditionally averaged flame index, ignoring locations with no flamelets, $\langle \xi_{LIF} | \xi_{LIF} \neq 0 \rangle$.

Figure 12. The average of ξ_{LIF}, a) $\langle \xi_{LIF} \rangle$, and conditional average, b) $\langle \xi_{LIF} | \xi_{LIF} \neq 0 \rangle$, where all locations without flamelets are ignored.
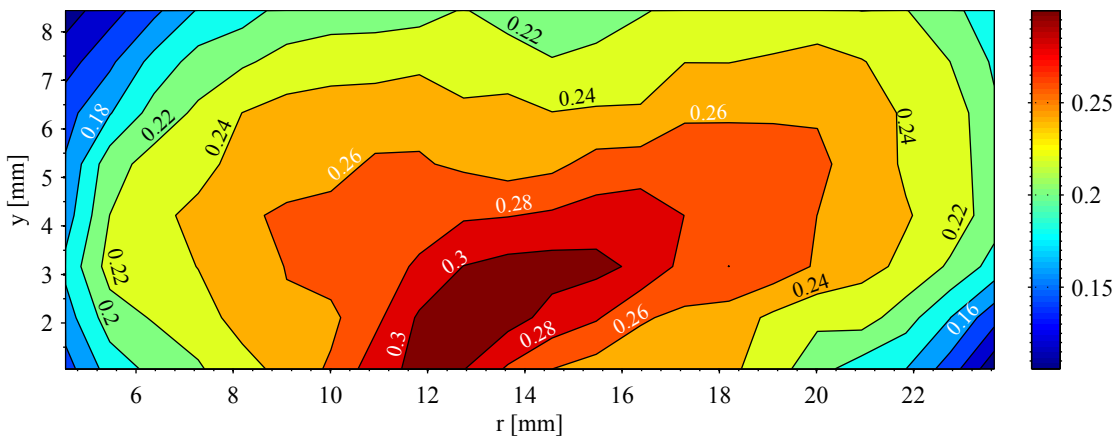

Figure 13. Standard deviation of ξ_{LIF}.

V. Discussion

Figure 12b shows that there in an enclosed (dark) region where we are more likely to see a non-premixed flame. This region lies between a height of 2 mm and 4 mm, and is between radial locations of 11 mm and 16 mm. In Fig. 12b premixed flamelets are likely to occur inside of the contour labeled 0.4. Also below about 2 mm, we have a high probability of seeing a premixed flame. The reason for the enclosed (dark) region of non-premixed flames in Fig. 12b is that pockets of pure fuel exist in this region. This was shown in Fig. 8b. The pockets of fuel are surrounded

American Institute of Aeronautics and Astronautics

by non-premixed flames.

Figure 12b demonstrates that premixed flamelets can also occur below the enclosed dark region of non-premixed flamelets. Previous studies[10,11] have shown that for this operating condition a combustion instability occurs with resonations taking place at 300 Hz. Coupled with this acoustic noise are large-scale fluctuations in flame shape and liftoff height. The liftoff height can vary such that the base of the flame lies below or up to 8 mm above the injector face. As the liftoff height oscillates, the fuel-air residence time between the injector nozzle and flame-base also varies. This fluctuation in residence time may result in various degrees of premixedness. In addition to changes in flame location, velocity fluctuations near the injector nozzle can alter the mixing mechanics of the combustor such that the flame index can drastically shift in time around this region.

VI.   Conclusion

A new measurement method has been developed and applied to measure the flame index in turbulent partially-premixed flames. The method used an NO_2 tracer gas added to the air and an acetone tracer added to the fuel. The PLIF signals from these tracer gases provided adequate signal to noise ratios.

Some instantaneous images of the flame index are reported as well as statistical information that can be useful for modeling purposes.

A.   Image Correction Theory

The PLIF signal captured by the cameras includes contributions from multiple sources other than the PLIF signal itself. Clemens[20] provides a method to isolate the PLIF signal from the other signals. If we consider $S_e(x,y)$ to be the signal for a given pixel that we wish to evaluate, we can relate S_e to the total signal acquired, S_{tot}, through the relationship:

$$S_{tot}(x,y,t_i,t_{ro}) = w(x,y)[L(y)S_e(x,y) + S_{back}(x,y,t_i)] + S_{dark}(x,y,t_{ro}), \qquad (9)$$

where $w(x,y)$ is the white-field response function, $L(y)$ is the laser sheet intensity distribution, S_{back} is the background signal, S_{dark} is the camera's dark noise, t_i is the exposure time, and t_{ro} is the array readout time. Rearranging Eq. (9) and solving for $S_e(x,y)$ gives a relation for the actual PLIF signal, which can be obtained through relatively straightforward processing:

$$S_e(x,y) = \frac{S_{tot}(x,y,t_i,t_{ro}) - [w(x,y)S_{back}(x,y,t_i) + S_{dark}(x,y,t_{ro})]}{w(x,y)L(y)}. \qquad (10)$$

The pixels on a CCD array do not have a uniform response to a given source of light, so $w(x,y)$ accounts for this non-uniformity. The white-field response was obtained by imaging a pane of frosted glass illuminated by fluorescent room lights, then rotating the camera 180° so that the pixels that imaged the bottom of the pane of glass, which was not as brightly lit as the top of the pane of glass, then imaged the top of the pane of glass. For each of these two conditions, 30 images were taken, and all 60 images were averaged. Taking the images under these two conditions corrected for any non-uniformity in the lighting of the pane of glass. The images were taken with the intensifier off and an exposure time of 2 ms on both of the Andor cameras. (A white-field correction was not performed on the camera that imaged the dye cell.) A white-field image acquired in this manner would have a lower signal at the edges of the image due to imaging with a circular aperture. This variation was corrected through the equation $I(\beta)/I(0) = \cos^4 \beta$, where β is the angle between the optical axis and a line connecting the center of the lens aperture to a given point on the object plane.[24] Prior to this correction, the dark-field response—obtained with the same exposure time as its respective white-field response—had to be subtracted from the white-field response.

The background signal, S_{back}, has contributions from the flame luminosity and from scattered laser light. However, when simultaneous PLIF is employed, fluorescence from both species may contribute. In this experiment the flame luminosity changed when acetone and NO_2 were present. So a method had to be devised that would provide a background image of the flame with acetone and NO_2, of when both the 532 nm and 266 nm lasers were operating, and of any possible fluorescence from the other tracer species[a]. In order to factor in these three contributions, three different background images were recorded for each camera. To obtain the luminosity of the flame with acetone and NO_2 present, a series of images was taken of the flame seeded with acetone and NO_2 but no lasers firing; this is called $S_{back_{FL}}$ (Background, Flame Luminosity). Ideally, a series of images could be captured that would include the fluorescence of the other tracer species and the laser light, but this was impossible without also a flame being present. (If no flame were present and the other tracer species were simply flowed into the burner, its fluorescence would exist

---

[a]The phrase "the other tracer species" is used to describe the tracer species the other camera was observing. In this case, acetone fluorescence for the NO_2 camera, and NO_2 fluorescence for the acetone camera.

in regions where if a flame had been present, the species would have been consumed.) In order obtain the needed conditions, a series of images was captured of the flame with the other tracer species present (e.g., a flame without NO_2 but with acetone, imaged by the NO_2 camera), and with both lasers on; this is called $S_{back_{FLnT,L}}$ (Background, Flame Luminosity no Tracer, Lasers). Then a third series of images was captured of the flame with only the other tracer species present (the same flame used to measure $S_{back_{FLnT,L}}$), with the lasers off; this signal is called $S_{back_{FLnT}}$ (Background Flame Luminosity no Tracer). An averaged $S_{back_{FLnT}}$ is then subtracted from an averaged $S_{back_{FLnT,L}}$ so that the resulting image would only have contributions from the scattered laser light and the fluorescence of the other tracer species (e.g., scattered 532 nm and 266 nm laser light as well as acetone fluorescence, for the NO_2 camera). The final background signal can be represented by:

$$S_{back} = S_{back_{FL}} + S_{back_{FLnT,L}} - S_{back_{FLnT}}. \tag{11}$$

It should be noted, however, that because the flow is unsteady, the luminosity from shot to shot is different. So each of the three background images was actually the average of 20 images taken under those conditions.

Except in the case of fully saturated fluorescence, the intensity of the fluorescence is dependent on spatial variations in the intensity of the laser sheet. These variations are accounted for by measuring $L(y)$, which is the profile of light intensity in the dye cell, and y is the vertical direction. L is considered to be a function only of y because the laser sheet was collimated upstream of both the dye cell and test section. In this experiment, a portion of the laser sheet was picked off and directed to a dye cell filled with an optically thick Rhodamine 6G solution, which was imaged for every laser pulse. A shot-to-shot laser sheet intensity correction was performed, rather than averaging the intensity over several images to obtain the correction. Examples of the profiles of laser sheet intensity are shown in Fig. 6. A knife edge was used to chop the edges of the laser sheet before the pick-off mirror to help align the laser sheet intensity correction with the PLIF signal. Both had a sharp drop-off in the signal at their edges.

S_{dark} is the dark-field response of the camera. It is the background signal count that exists with no light source. The dark-field response is dependent on the exposure time and readout time of the CCD. Dark-field images were taken with the same exposure time and readout time as the data image.

If the background image was obtained with the same camera as the S_{tot}, then Eq. (10) can be rewritten as:

$$S_e = \frac{S_{tot} - S_{correction}}{wL}, \tag{12}$$

where $S_{correction} = wS_{back} + S_{dark}$. The background images already take into account the contributions due to the white-field and dark-field found in the numerator of Eq. (10) because w and S_{dark} remain constant for different images with the same exposure time and readout time. Technically, $S_{correction}$ is the background image itself, while S_{back} is one component of that correction, The others are the white-field and dark-field corrections.

Due to the fact that a shot-to-shot correction was used, the laser sheet intensity correction for the PLIF image, S_{tot}, and for the background image, $S_{back_{FLnT,L}}$, were different. From Eq. (11) and Eq. (10), we obtain the full relation for the corrected PLIF signal:

$$S_e = \frac{S_{tot}}{wL_1} - \frac{wS_{back_{FL}} + S_{dark}}{w} - \frac{wS_{back_{FLnT,L}} + S_{dark}}{wL_2} + \frac{wS_{back_{FLnT}} + S_{dark}}{w}, \tag{13}$$

where L_1 is the laser sheet intensity corrections for the acquired PLIF image. L_2 is the sheet correction for the background signal obtained with the flame seeded only with the tracer species that the other camera was observing. It should also be noted that there is no laser sheet intensity correction on the other two background correction terms. This is because those images were acquired without the lasers firing, so there was no laser sheet to correct for.

Equation. (13) can be simplified if it is rewritten in terms of the background images that were actually acquired:

$$S_e = \frac{S_{tot}}{wL_1} - \frac{S_{FL}}{w} - \frac{S_{FLnT,L}}{wL_2} + \frac{S_{FLnT}}{w}, \tag{14}$$

where S_{FL}, $S_{FLnT,L}$, and S_{FLnT} are the acquired background images that include the background signals $S_{back_{FL}}$, $S_{back_{FLnT,L}}$, and $S_{back_{FLnT}}$, respectively.

Finally, Eq. (14) can be simplified if the background terms are combined as:

$$S_B = \frac{S_{FL}}{w} + \frac{S_{FLnT,L}}{wL_2} - \frac{S_{FLnT}}{w}, \tag{15}$$

where S_B is the combined background image.

So, if Eq. (15) is combined with Eq. (14), we obtain the final equation used to correct the acquired PLIF images in this experiment,

$$S_e = \frac{S_{tot}}{wL_1} - S_B. \tag{16}$$

Acknowledgments

References

[1]Yamashita, H., Shimada, M., and Takeno, T., "A numerical study on flame stability at the transition point of jet diffusion flames," *Proc. Combust. Inst.*, Vol. 26, No. 1, 1996, pp. 27–34.

[2]Fiorina, B., Gicquel, O., Vervisch, L., Carpentier, S., and Darabiha, N., "Approximating the chemical structure of partially premixed and diffusion counterflow flames using FPI flamelet tabulation," *Combust. Flame*, Vol. 140, No. 3, 2005, pp. 147–160.

[3]Knudsen, E. and Pitsch, H., "A general flamelet transformation useful for distinguishing between premixed and non-premixed modes of combustion," *Combust. Flame*, Vol. 156, No. 3, 2009, pp. 678–696.

[4]Domingo, P., Vervisch, L., and Rveillon, J., "DNS analysis of partially premixed combustion in spray and gaseous turbulent flame-bases stabilized in hot air," *Combust. Flame*, Vol. 140, No. 3, 2005, pp. 172–195.

[5]Domingo, P., Vervisch, L., and Bray, K., "Partially premixed flamelets in LES of nonpremixed turbulent combustion," *Combust. Theor. Model.*, Vol. 6, No. 4, 2002, pp. 529–551.

[6]Mizobuchi, Y., Tachibana, S., Shinio, J., Ogawa, S., and Takeno, T., "A numerical analysis of the structure of a turbulent hydrogen jet lifted flame," *Proc. Combust. Inst.*, Vol. 29, No. 2, 2002, pp. 2009–2015.

[7]Ferraris, S. A. and Wen, J. X., "Large eddy simulation of a lifted turbulent jet flame," *Combust. Flame*, Vol. 150, No. 4, 2007, pp. 320–339.

[8]Knudsen, E. and Pitsch, H., "Capabilities and limitations of multi-regime flamelet combustion models," *Combust. Flame*, Vol. 159, No. 1, 2012, pp. 242–264.

[9]Giezendanner, R., Weigand, P., Duan, X. R., Meier, W., Meier, U., Aigner, M., and Lehmann, B., "Laser-based investigations of periodic combustion instabilities in a gas turbine model combustor," *J. Eng. Gas Turb. Power*, Vol. 127, No. 3, 2005, pp. 492–496.

[10]Weigand, P., Meier, W., Duan, X., Stricker, W., and Aigner, M., "Investigations of swirl flames in a gas turbine model combustor: I. Flow field, structures, temperature, and species distributions," *Combust. Flame*, Vol. 144, No. 1-2, 2006, pp. 205–224.

[11]Allison, P. M., Driscoll, J. F., and Ihme, M., "Acoustic characterization of a partially-premixed gas turbine model combustor: Syngas and hydrocarbon fuel comparisons," *Proc. Combust. Inst.*, (to be published).

[12]Rosenberg, D. A. and Driscoll, J. F., "A method to image flame index in partially premixed flames," *50th AIAA Aerospace Sciences Meeting*, AIAA Paper 2012-0972, Nashville, TN, 2012.

[13]Lozano, A., Yip, B., and Hanson, R. K., "Acetone: a tracer for concentration measurements in gaseous flows by planar laser-induced fluorescence," *Exp. Fluids*, Vol. 13, No. 6, 1992, pp. 369–376.

[14]Thurber, M. C. and Hanson, R. K., "Pressure and composition dependences of acetone laser-induced fluorescence with excitation at 248, 266, and 308 nm," *Appl. Phys. B*, Vol. 69, No. 3, 1999, pp. 229–240.

[15]Schulz, C. and Sick, V., "Tracer-LIF diagnostics: quantitative measurement of fuel concentration, temperature and fuel/air ratio in practical combustion systems," *Prog. Energy Combust. Sci.*, Vol. 31, No. 1, 2005, pp. 75–121.

[16]Agarwal, Y., Hadeishi, T., and Robben, F., "Measurement of NO_2 concentration in combustion using fluorescence excited by an argon-ion laser," *14th AIAA Aerospace Sciences Meeting*, AIAA Paper 76-0136, Washington, DC, 1976.

[17]Donnelly, V. M., Keil, D. G., and Kaufman, F., "Fluorescence lifetime studies of NO_2. III. Mechanism of fluorescence quenching," *J. Chem. Phys.*, Vol. 71, No. 2, 1979, pp. 659–673.

[18]Cattolica, R. J., "Visualization of flame propagation by laser-fluorescence imaging of nitrogen dioxide," *Combust. Sci. Technol.*, Vol. 54, No. 1-6, 1987, pp. 61–67.

[19]Cattolica, R. J., "Combustion-torch ignition: fluorescence imaging of NO_2," *Proc. Combust. Inst.*, Vol. 21, No. 1, 1988, pp. 1551–1559.

[20]Clemens, N. T., *Encyclopedia of Imaging Science and Technology*, chap. Flow Imaging, John Wiley & Sons, Inc., 2002, pp. 390–419.

[21]Partridge, Jr., W. P. and Laurendeau, N. M., "Formulation of a dimensionless overlap fraction to account for spectrally distributed interactions in fluorescence studies," *Appl. Opt.*, Vol. 34, No. 15, 1995, pp. 2645–2647.

[22]Perona, P. and Malik, J., "Scale-space and edge detection using anisotropic diffusion," *IEEE Trans. Pattern Anal. Mach. Intell.*, Vol. 12, No. 7, 1990, pp. 629 –639.

[23]Canny, J., "A computational approach to edge detection," *IEEE Trans. Pattern Anal. Mach. Intell.*, Vol. PAMI-8, No. 6, 1986, pp. 679–698.

[24]Smith, W. J., *Modern Optical Engineering: The Design of Optical Systems*, McGraw Hill, New York, 4th ed., 2008.

American Institute of Aeronautics and Astronautics